Theoretical perspectives on the dynamics of great red spot and self-organized vortices in Jupiter's atmosphere

Umer Rehman[a*,b,c] , Muhammad Mubashir Israr[a], Ibrar Hussain[d], Nisar Ahmad[e]

[a] *Department of Physics, Air University E-09 Sector 44000 Islamabad, Pakistan.*
[b]*School of Astronomy and Space Science, Nanjing University, Nanjing 210093, China.*
[c]*Key Laboratory of Modern Astronomy and Astrophysics (Nanjing University), Ministry of Education, China.*
[d]*Department of Physics, University of Wah, Wah Cantt. 47040 Rawalpindi, Pakistan.*
[e]*College of Science, Harbin Institute of Technology (Shenzhen), Shenzhen 518055,China.*
[*]*Authors to whom any correspondence should be addressed. E-mail: umer@mail.ustc.edu.cn*

Abstract

Based on data from the WFC3/UVIS instrument on board the Hubble Space Telescope (HST), we presented a theory describing the effect of zonal jets in the Great Red Spot (GRS) of Jupiter. The charged dust cloud and neutrals with background of un-bounded plasma is used as a modelling tool for driven-dissipative complex flow systems in nature. We predicted structural variations of self-organized vortices in Jupiter's atmosphere, such as the GRS and White Ovals. The steady state flow linear and nonlinear solutions are obtained using a 2D hydrodynamic model. The steady driven dust circulation of the vortices in Jupiter's atmosphere are revealed by these linear and nonlinear solutions. Inner structural changes connected to driving fields rather than kinematic viscosity, it is demonstrated that high-speed collar rings that are persistent around the uniform vorticities of the GRS. This analysis also illuminates the role played by the driving field, boundaries, and Jovian parameter in establishing the typical size, circulation direction, strength, and drift of the vortices in atmosphere of Jupiter.

Keywords: Jupiter's atmosphere, Great Red Spot, Hydrodynamics Model, Hubble Space Telescope

1. Introduction

The atmosphere of Jupiter, the largest planet in the solar system, supports a variety of dynamical behavior, ranging from micro-level turbulence and instabilities to macro-scale stable zonal jets and vibrant vortices (Marcus, 1993; Marcus, 1993; Vasavada et al., 1998). The Great Red Spot (GRS), White Ovals, as well as band structured Belts and Zones connected with the sheared zonal jets are the most prominent aspects in atmosphere of Jupiter (Simon et al., 2014; Choi, et al., 2010; Marcus and Shetty, 2011). At central latitude 22.3^0 S of Jupiter (where 1° = 1160 km), the GRS is an

incredible, enduring large anticyclone cloud vortex with dimensions of 14.1° longitude and 9.4° latitude (Simon et al., 2018), while the White Ovals are comparatively small vortices seen at latitudes 33.8° S, 41.8° S, and 19.0° N (Vasavada et al., 1998; Choi et al., 2010; Marcus and Shetty, 2011). White Ovals and GRS both have dormant central regions of symmetric vorticity surrounding by collar rings of fast flow that separate the central regions from adjacent feeble flows (Vasavada et al., 1998; Mitchell, et al., 1981).

The previously observed characteristics in atmosphere of Jupiter have been confirmed by NASA's spacecraft (Juno-2018) including the interior rotating period of GRS is decreasing, the giant vortex is contracting at a rate of 0.19°/year along latitude and 0.048°/year along longitude. The inclusive shape is becoming more circular with passage of time and barely noticeable changes in the flowing zonal jets are seen (Simon et al., 2014; Simon, et al., 2018). Many mysteries adjoining the physical explanation in vortices of Jupiter such as the driving mechanism, drift of GRS on the plane, the continual shape change, the existence of collar rings of fast flow in the dormant core, the long-lasting perseverance of the vortices, and the actual 3D shape, among others are still unrevealed even subsequently several decades of observations and analysis (Vasavada et al., 1998; Simon et al., 2014; Rogers, 2008; Simon-Miller, et al., 2002). The shape and long-term sustainability in GRS of Jupiter render it distinctive among vortices that are generate on the other planets in our solar system. Nevertheless, it additionally behaves as a stereotype in a category of "pancake vortices" that are anticyclones with the background of fluids (steadily flowing). Rendering to theoretical explanations of laboratory experiments and data of velocity fields in Jovian vortex, pancake vortices have a width that is considerably lesser than their horizontal dimensions. According to Sun et al., 2018 both exciting (turbulence) and trapping (bulk transport) mechanisms are used by terrestrial ocean eddies to convey heat meridionally. Though trapping could be considerable on Saturn, where pole-ward migration of the anticyclone produced by the 2010 Great White Storm (Hueso et al., 2020; Sayanagi et al., 2013). On the other hand, trapping could not be ensured on Jupiter due to main vortices being surrounded by jets that bound meridional migration. Marcus, 2004 anticipated that the exciting mechanism, which is governed by the chaotic behavior of three white ovals close to 34° S at Jupiter, could transform, possibly resulting in a change in temperature at that latitude. But the evidence is questionable given that later Oval changed its color back to white (Simon, 2015). It may be possible to analyze different planetary fluid systems, from the fluids on small planets to the atmospheres of gigantic planets by

studying the evolution of vortices across time. Recently, Wong et al. 2021 acquired Data by HST/WFC3 (Dressel, 2021) over the time period 2009–2020 and used the Advection Corrected Correlation Image Velocimetry (ACCIV) method to recover the velocity field. This method was created specifically to measure velocities along curved routes in Jupiter's anticyclones (Asay-Davis et al., 2009; Asay-Davis, 2015). Although the region just outside the high-speed ring is also a part of the vortex, they adopt the ring of high-speed winds as the definition of the vortex dynamical border since it best describes the overall dynamical structure of the GRS.

Several fluid models that include the concept of potential vorticity deduce vortices as Rossby solitons. The flow profiles, ongoing structural variations and horizontal drift velocity are only a few of the many critiques that have been levelled with this concept (Marcus and Lee, 1994; Dowling and Ingersoll, 1989). Additionally, it has been suggested that the energy from small-scale eddies and moist convection from the deep interior of Jupiter's interior drive both the streaming zonal jets and the vortices of its atmosphere (Ingersoll et al., 2000). However, it is unlikely that these processes are the primary causes of such massive vortices. The actual mechanisms underlying the dynamics and distinctive features of these vortices are still unknown. The GRS and White Ovals, on the other hand, are described as complex flow systems made up of a variety of species, including NH_3, CH_4, Ar, NH_4SH, H_2O-ice, dust and charged particles that are in dynamic equilibrium with the zonal jets and other forcing factors like the Coriolis force and thermo-convection moist (Marcus, 1993; Loeffler et al., 2016; Weidenschilling and Lewis, 1973). Moreover, the position and shear intensity of the streaming jets, which think to be the primary source of the vortices on Jupiter are significantly connected with the size, strength, and direction of the vortices in the planet's banded structure (Vasavada et al., 1998; Choi, et al., 2010; Mitchell, et al., 1981; Rogers, 2008). It has been demonstrated that GRS has extensive relatively stable vertically divided deeper layers inside of thin, wide upper layers, which have minimal effect on the dynamics of the uppermost layers (Marcus, 1993; Vasavada et al., 1998).

The major goal of this study is to give the theory that describes the dynamical characteristics of the GRS, which is based on data (Wong et al. 2021) from the WFC3/UVIS instrument on board the Hubble Space Telescope (HST). We presented mathematical model that analyzed the charged dust cloud's linear and nonlinear behavior in an environment with unbounded streaming plasma similar to the GRS. In reality, higher dimensional nonlinear partial differential

equations (NPDEs) should be used to represent the linear and nonlinear dynamics of the real planetary atmosphere. The KdV equation and the mKdV equation in (2 + 1) dimensional situations have been examined by several researchers in a variety of scientific fields, including plasma physics, space science, ion-acoustic waves, shallow water waves, and others (Kadomtsev and Petviashvili, 1970; Groves and Sun, 2008; Infeld and Rowlands, 2001; Zakharov and Kuznetsov, 1974). It is commonly known that the (2 + 1) dimensional model equations of Kadomtsev-Petviashvili and Zakharov-Kuznetsov are used to describe shocks, solitons and vortex dynamics (Kadomtsev and Petviashvili, 1970; Zakharov and Kuznetsov, 1974). These models effectively explain the underlying physical phenomena. The meridian gradient of planetary vorticity is responsible for the existence of planetary Rossby-waves. The existence of vortex Rossby-waves on the storm's radial gradient was proposed. Guinn and Schubert 1993 study was a significant step forward in the understanding of hurricane spiral bands. Still many issues about their dynamical aspects remain unsolved. For instance, is the symmetrization process accompanied by fine-scale outward propagating waves? If so, is it possible to predict their key features, such as phase and group velocity, eddy-momentum flux, and interaction between waves and mean flows? In this study, we took vortex axisymmetrization into account by creating a wave mechanics that combines the theories of barotropic vortex axisymmetrization and vortex Rossby-wave propagation in fast rotating vortices. The theory established here explains the GRS's dynamical behavior. The theory offers analytical and numerical calculations that give dispersion relations, linear and nonlinear solutions for phase and group velocities that are employed as indicators of vortex Rossby waves in observational data. A mechanism for the interaction of wave-mean-flow for vortex intensification is additionally demonstrated by the theory. This process might have a significant impact on structural variations.

The arrangement of the article is as follows. We focus on theory, geometry description, derivation of dispersion relation, and presentation of the linear and nonlinear governing equations in section 2. We present the auxiliary equation explanations and results are discussed using a numerical solution in section 3. In section 4, some conclusions are presented.

2. Theory

Consider the dynamics of the GRS as a bounded cloud made up of charged dust, neutrals, and plasma that behaves isothermally and incompressible and has a geometry in the Cartesian

coordinate system. The z-axis is the center of the ball to the point on plane, the direction is outward and perpendicular to the plane xy. The x-axis is tangent to the left of the point and the direction points to the east (Longitude). The y-axis along the direction of the north (Latitude). The movement of the fluid can be seen approximately on xy (2-dimensional) motion on the plane (See Wong et. al., 2021 for a more thorough illustration of the geometry). The governing equation of the dynamics of dust flows that satisfy the incompressibility condition and have finite viscosities is given as

$$\frac{\partial \boldsymbol{u}}{\partial t} + (\boldsymbol{u} \cdot \nabla)\boldsymbol{u} = -\frac{\nabla p}{\rho} + \mu \nabla^2 \boldsymbol{u} - 2\boldsymbol{\Omega} \times \boldsymbol{u} - \chi(\boldsymbol{u} - \boldsymbol{v}) - \eta(\boldsymbol{u} - \boldsymbol{w}) + \frac{e}{\rho}\nabla\phi \qquad (1)$$

The above equation can be used to accurately account for both the drive given by ion drag and the friction caused by stationary neutral fluids (Landau and Lifshits, 1987).The flow velocities of the dust, ions, and neutral fluids are represented here by $\boldsymbol{u}$, $\boldsymbol{v}$, and $\boldsymbol{w}$, respectively. Where, $\boldsymbol{\Omega}$ is the angular velocity, p is the pressure, ρ is mass density of the dust fluid, μ is the kinematic viscosity, χ coefficient of ionic drag on the dust and η is the coefficient of friction produced by the stationary neutral fluid (Barnes et al., 1992; Khrapak et al., 2002; Ivlev et al. 2004). While the electrons are in thermal equilibrium with the streaming ions and the confined dust, the last term is representing the electrostatic force of dust-plasma environment. In the coordinate system with the planetary rotational motion, the fluid element is subjected to the usual pressure (first term on r.h.s in Eq. 1), viscous effects (second term on r.h.s in Eq. 1), and is also affected by the Coriolis force (third term on r.h.s in Eq. 1). The entire mix of charged dust, neutrals and background plasma is quasi-neutral. The expression ensures that the confined dust component incompressible is expressed as

$$\nabla \cdot \boldsymbol{u} = 0 \qquad (2)$$

The fluid element has two components of velocity that are given as subject to the geometry mentioned above,

$$\boldsymbol{u}(\boldsymbol{x}, \boldsymbol{y}) = U\hat{\boldsymbol{x}} + V\hat{\boldsymbol{y}} \qquad (3)$$

The relationships mentioned above allow for the definition of a stream function $\boldsymbol{u} = \nabla\psi \times \hat{\boldsymbol{z}}$ where the associated velocity components are given as

$$U = \frac{\partial \psi}{\partial y} \text{ and } V = -\frac{\partial \psi}{\partial x} \tag{4}$$

The geometric effects of the sphere in three dimensions can be made simpler by β plane approximation; at a specific latitude of the rotating sphere small angle approximation is used. Take a small angle deviation and use the point as a cut plane for spherical shaped planet we get,

$$sin(\theta_0 + \delta\theta) \sim \sin\theta_0 + \frac{cos\theta_0 y}{R} \tag{5}$$

where, $\delta\theta = y/R$ is used. Here, y is the variation across the latitude, R is the radius of the planet, and θ is the angular relationship between the vector of the fluid element and the equatorial plane.

A. Linear Analysis

Eq. (1) and (2) are linearized under the definition of Eq. (3) and expressed in the form of components in Cartesian coordinate system,

$$\frac{\partial U}{\partial t} = -\rho_0^{-1}\frac{\partial p}{\partial x} + \mu\frac{\partial^2 U}{\partial x^2} + 2\Omega V \sin\theta + \frac{e}{\rho_0}\frac{\partial}{\partial x}\phi \tag{6}$$

$$\frac{\partial V}{\partial t} = -\rho_0^{-1}\frac{\partial p}{\partial y} + \mu\frac{\partial^2 V}{\partial y^2} + 2\Omega U \sin\theta + \frac{e}{\rho_0}\frac{\partial}{\partial x}\phi \tag{7}$$

$$\frac{\partial U}{\partial x} + \frac{\partial V}{\partial y} = 0 \tag{8}$$

Here, ρ_0^{-1} is the background density of the fluid element. Realistic scenarios in the GRS environment indicate that χ and η has minimal effect and can be ignored. The last terms on the r. h. s of Eq. (6) and (7) is evaluated in β plane using Eq. (5), which can be written as,

$$2\Omega \sin\theta = 2\,\Omega\sin\theta_0 + 2\,\Omega\,\frac{cos\theta_0 y}{R} \tag{9}$$

$$\Rightarrow 2\Omega\sin\theta = f_0 + \beta y \tag{10}$$

In Eq. (10), β is a constant for the chosen coordinate origin, or the plane's origin. It is possible to represent the three-dimensional motion of the fluid on the revolving sphere as a two-dimensional motion in the plane. For angular variables $\beta = d(2\Omega_z)/dy$ (where, $\Omega_z = \Omega sin\theta$) is used. Using β plane approximation, Eq. (6) and (7) can be written as

$$\frac{\partial U}{\partial t} - f_0 V - \beta V y = -\rho_0^{-1}\frac{\partial p}{\partial x} - \mu\frac{\partial^2 U}{\partial x^2} + \frac{e}{\rho_0}\frac{\partial}{\partial x}\phi \tag{11}$$

$$\frac{\partial V}{\partial t} + f_0 U + \beta U y = -\rho_0^{-1}\frac{\partial p}{\partial y} + \mu\frac{\partial^2 V}{\partial y^2} + \frac{e}{\rho_0}\frac{\partial}{\partial x}\phi \tag{12}$$

These equations are coupled in U and V, and decoupling them yields independent equations for these variables. One can derive a decoupled equation and represent it as

$$\frac{\partial \nabla U}{\partial t} - \beta\frac{\partial U}{\partial x} - \gamma\frac{\partial^2 \nabla U}{\partial x^2} + \mu\frac{\partial^3 U}{\partial x^3} = 0 \tag{13}$$

Where, $\gamma = (1/n)\sqrt{kT/M}$ is originated from the fact of overall charged neutrality condition of the plasmas. The dust grain initially gets negatively charged because the ion current to it is substantially less than the electron current. This causes the electron and ion currents to fluctuate until electron current and ion current are equalized $j_e = j_i$, where $j_e = n_e e\sqrt{kT/m_e}\left(e^{e\phi/kT}\right)$ and $j_i = n_i e\sqrt{kT/M}(1 - e\phi/kT)$, all symbols have usual meaning (Barken et al. 1995: Rehman 2022). The factor $1 - e\phi/kT$ is caused by orbital motion effects has been implemented. The second term in Eq. (13) is origin of rotating sphere, the third is representing the electrostatic force contribution and the last term narrating the viscous force effect. We can present above equation in terms of stream function ψ to obtain the solution of this second order partial differential equation for the GRS environment,

$$\frac{\partial}{\partial t}(\nabla_\perp^2\psi) - \beta\frac{\partial \nabla_\perp \psi}{\partial x} - \gamma\frac{\partial^2}{\partial x^2}(\nabla_\perp^2\psi) + \mu\frac{\partial^3 \nabla_\perp \psi}{\partial x^3} = 0 \tag{14}$$

Here, $\nabla_\perp^2 = \partial^2/\partial x^2 + \partial^2/\partial y^2$ is the two-dimensional non-divergent viscous flow on an β-plane is the model used as a prototype implies precisely planetary atmospheric vortices. More details are considered in section 3. Considering the parameters from the data base article (Wong et. al. 2021) along with the dimensionless parameters are introduced as $(x, y) = L_0(x', y')$, $t = L_0 t'/U_0, \psi = L_0 U_0 \psi', \beta = U_0\beta'/L_0^2$, and $\mu = U_0\mu'/L_0$. Furthermore, assuming the oscillatory solution $\sim \exp\left[\mathrm{i}\left(k_x x + k_y y - \omega t\right)\right]$of the Eq. (14), the dispersion relation of the linear wave can be obtained as,

$$\left(k_x + \frac{\beta}{2\omega}\right)^2 + k_y^2 - \gamma k_x^2 k_y^2 + \mu k_x^3 = \left(\frac{\beta}{2\omega}\right)^2 \tag{15}$$

This is the dispersion relation of the wave, which is known as the linear solution of rotating fluid and can reproduced well known Rossby wave if electrostatic force due to charged particle is

ignored. The wave is exclusive to rotating fluids. The absence of this wave occurs when the sphere is not rotating.

B. Nonlinear Analysis

A simple set of equations is produced by keeping the convective nonlinear term in the momentum equation of the fluid Eq. (1) with all same assumption made in above section and applying the beta plane approximation. We get,

$$\frac{\partial U}{\partial t} + \mathrm{U}\frac{\partial U}{\partial x} + +\mathrm{V}\frac{\partial U}{\partial y} - f(y)V = -\rho_0^{-1}\frac{\partial p}{\partial x} - \mu\frac{\partial^2 U}{\partial x^2} + \frac{e}{\rho_0}\frac{\partial}{\partial x}\phi \quad (16)$$

$$\frac{\partial V}{\partial t} + \mathrm{U}\frac{\partial V}{\partial x} + +\mathrm{V}\frac{\partial V}{\partial y} - f(y)U = -\rho_0^{-1}\frac{\partial p}{\partial y} + \mu\frac{\partial^2 U}{\partial y^2} + \frac{e}{\rho_0}\frac{\partial}{\partial x}\phi \quad (17)$$

where $f = f_0 + \beta y$ is the Coriolis parameter. Coriolis force leads to the vector nonlinear term, eventually forming a self-organizing structure. Using the expression from Eq. (2) to (4), we can express momentum balance equation in vector form as

$$\frac{\partial}{\partial t}(\nabla\psi \times \hat{z}) + (\nabla\psi \times \hat{z}).\nabla(\nabla\psi \times \hat{z}) + f(y) \times (\nabla\psi \times \hat{z}) = -\rho_0^{-1}\nabla\vec{p} + \mu\nabla^2(\nabla\psi \times \hat{z}) \quad (18)$$

After doing some simple algebraic manipulations and substitution we get term by term expressions

$$\frac{\partial}{\partial t}\nabla \times (\nabla\psi \times \hat{z}) = -\frac{\partial}{\partial t}\nabla^2\psi\hat{z} \quad (19)$$

$$\nabla \times (\nabla\psi \times \hat{z}).\nabla(\nabla\psi \times \hat{z}) = (\nabla\psi \times \hat{z}) \cdot \nabla\nabla^2\psi \quad (20)$$

$$\nabla \times f(y) \times (\nabla\psi \times \hat{z}) = -\beta\frac{\partial\psi}{\partial x}\hat{z} \quad (21)$$

Putting expressions Eq. (19) to (21) in Eq. (18) and implying dimensionless parameters as$(x, y) = L_0(x', y')$, $t = L_0 t'/U_0$, $\psi = L_0 U_0 \psi'$, $\beta = U_0\beta'/L_0^2$, and $\mu = U_0\mu'/L_0$we get NPDE for the GRS environment as

$$\frac{\partial}{\partial t}\nabla^2\psi + (\hat{z} \times \nabla\psi) \cdot \nabla\nabla^2\psi + \beta\frac{\partial\psi}{\partial x} = 0 \quad (22)$$

A class of two-dimensional flow has been taken into account in this work. The Charney—Hasegawa—Mima equation, in which the vorticity is proportional to the stream function (SHIVAMOGGI, 1989), appears to be analogous to above Eq. (22). A uniform stream disrupts a

metastable equilibrium of rotating fluid composed of charged dust, neutral and plasma. For these flows that reflect a disturbance over a uniform stream, we are able to get NPDE numerical solutions. Section 3 of this article provides more information on the numerical solutions.

3. Results and Discussion

We employ several equations in Figs. (1) to (5) to quantify the linear and nonlinear amplitude of Modified Rossby waves. According to the given parameters, it is demonstrated that the evolution of wave amplitude follows similar laws in the x (along longitude) and y (along latitude) directions. Identifying propagating waves from the mathematical solution is challenging. However, by looking at the manner in which wave number one's symmetries change on a basic-state velocity profile, the wave mechanics may still be comprehended. The relative vorticity map, the scattered-vector velocity fields, the gridded velocity field, and cuts through the principal axes of the vortex are all part of the velocity field we obtained from the article data based on WFC3/UVIS instrument on board the HST (Dressel, 2021).The mean absolute value of the relative vorticity is taken $10^{-5}s^{-1}$in the outer region throughout the timeline for the relative vorticity map of the GRS as well as the size and shape of the high-speed ring. While other used parameters are $L_x{\sim}10^6\ km$ zonal length scale, $L_y{\sim}10^5\ km$, meridional length scale, $H{\sim}10^2\ km$ atmosphere height, g = 24.79 $m.sec^{-2}$ gravity of the Jupiter, $L_0{\sim}10^6 km$ is the zonal characteristic length, U_0 is the characteristic zonal velocity scale inserted from the available onboard data (Wong et al., 2021).

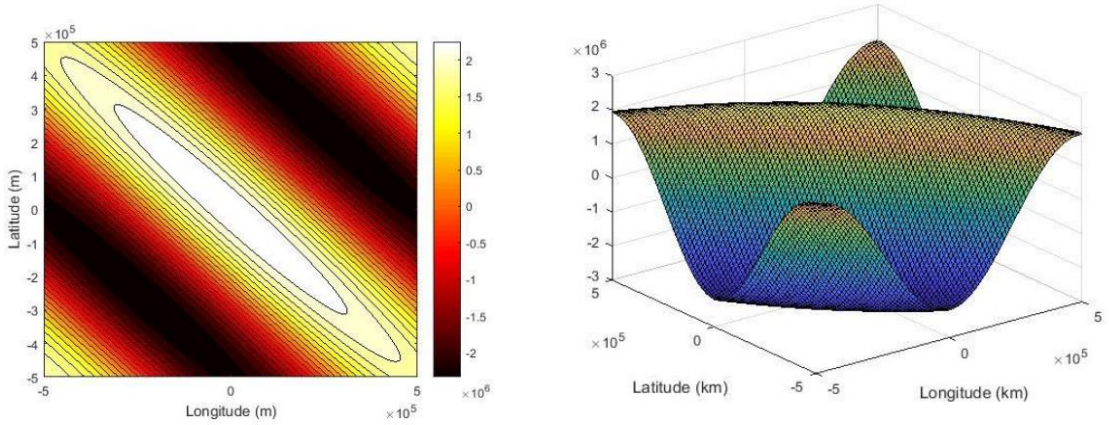

Figure 1: Numerical solution of Eq. (14) displays longitude, latitude, and steam functions (Contour on left and 3D on right) at zonal velocity scale 〖U〗_0=120 m/sec of the GRS.

We have numerically solved Eq. (14), where characteristic length- and velocity-scales correspond to the radius of maximum winds (RMW) and the maximum tangential velocity, respectively as given (Wong et al., 2021). The solution has been obtained by assuming the Rossby solution method as described in Liu et al., 2018. Plot in Fig. 1 (Contour on left and 3D on right) displays longitude, latitude, and steam functions at zonal velocity scale $U_0 = 120\, m/sec$ of the GRS. The vortex satisfies Rayleigh's necessary condition for exponential stability because the mean vorticity is a monotonic function of radius (Gent and McWilliams 1986). The conclusions have been validated for various swirl solutions with finite energy and angular momentum, despite the fact that this vortex contains integrated kinetic energy and angular momentum. Outward-propagating waves frequently have length-scales that are less than the typical radial scale L_0 of the vortex. According to the behavior of the solution and the numerical results for the given zonal velocity, Fig. 1 depicts the plot for the solution (contour on the left and 3-dimensional on the right), which unmistakably depicts outward-propagating wave-packets. There are three more noteworthy characteristics. The first is that individual packets have a tendency to expand quickly as they go outward. Secondly, the stream function exhibits non-monotonic behavior. Thirdly, wave dispersion is seen in the group-velocity for individual packets, which shows a relationship on wavelength. In stable vortex-flows, this solution illustrates a crucial wave process by which disturbances can take energy out of the vortex at one band and deposit it at another. The detailed analysis on the wave dispersion is shown in Fig. 2.

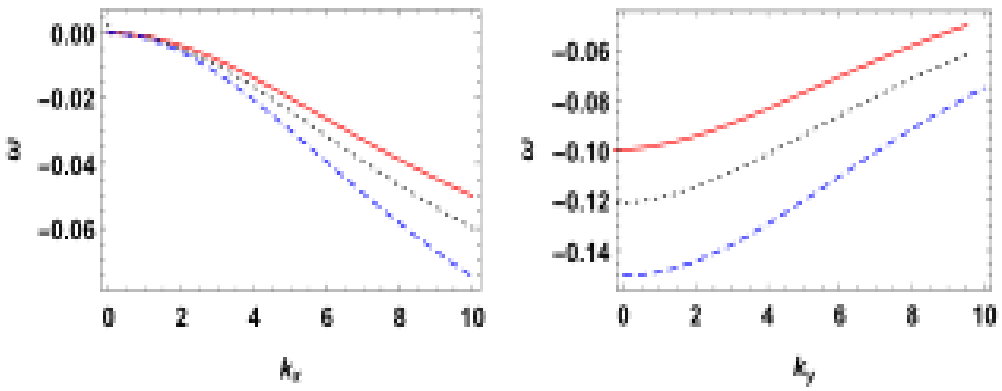

Figure 2: Variation of the mode frequency ω over a range of wave-number k_x (left) and k_y (right) generated from the dispersion relation Eq. (15) at ϕ→0.

The modes of oscillation from the dispersion relation Eq. (15) have been numerically solved to describe the stability of self-organized vortex. The root of Eq. (15), which describes how waves in a vortex disperse, provides an explanation about the stable vortex. In Fig 2 the frequency of mode ω as a function of wavenumber k_x(on the left) and k_y(on the right) is plotted, where $k_x = 2\pi/L_0$ and $k_y = 2\pi/L_0$ is implemented. The variation in plot showing that the frequency of the mode decreases as a function of k_x (on the left), and increases as a function of k_y(on the right). Trending is exactly justifying above statement on energy exchange. No imaginary root of Eq. (15) can be obtained from the dispersive characteristics, demonstrating the absence of the unstable mode that would guarantee the stability of the vortex with respect to dissipative mechanism. However, zonal velocity flow and vorticity can be used to support the vortex's shirking (which is very slow peace mechanism). The frequency of the mode trends monotonically with wavenumber. A completely stable oscillation spectrum is found. The illustration of the influence of kinematics viscosity on dispersive wave propagation is also explored in Fig. 2 without considering the electrostatic effect at $\phi \to 0$ by subsiding third term in Eq. (15). The variation in frequency obtained at three different values of kinematic viscosity corresponding to Jupiter atmosphere at $10^7 m^2/sec$,$2 \times 10^7 m^2/sec$, and $5 \times 10^7 m^2/sec$ (Vidmachenko, 1986) , are depicted as solid red, dotted black, and dashed blue curves, respectively. When the kinematic viscosity μ is raised while the vorticity remains constant, the frequency of decreases as function wavenumber. However, the illustration of finite electrostatic effect on dispersive wave propagation is playing very significant role in the linear wave dynamics as shown in Fig. 3.

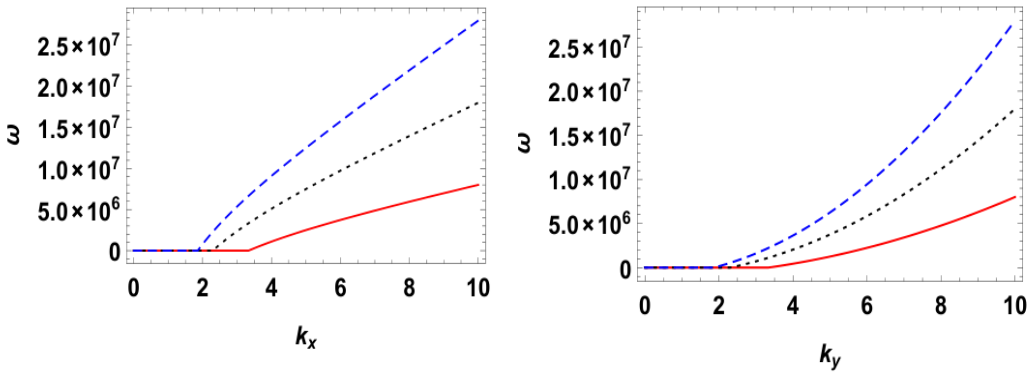

Figure 3: Variation of the mode frequency ω over a range of wave-number k_x (left) and k_y (right) generated from Eq. (15) at three different values of γ.

The variation in frequency obtained at three different values of γ to Jupiter atmosphere at $\gamma = 0.1, \gamma = 0.2$ and $\gamma = 0.3$ are depicted as solid red, dotted black, and dashed blue curves, respectively. When the concentration of plasma particle is raised while the vorticity and viscosity remains constant, the frequency of the wave increase as function of wavenumber and oscillations get propagate at lower value of k_x and k_y. The analytical dispersion relation (15) has been being evaluated by parametric analysis. A numerical solution is found for the frequency of the mode. The frequency spectrum of the mode as it varies with respect to k_x and k_y is depicted in three dimensions as shown in Fig. 4. The ranges for the values of k_x and k_y determine the mode frequency, which ranges $0 \leq k_x, k_y \leq 10$ from zero to the maximum oscillates in k_x and k_y. Two mutually perpendicular propagating wave-vector contributed exactly equal amount of wave frequency of the mode at $k_x = k_y = 10$. The stable oscillation are found in the range $2 \leq k_x \leq 4$ *and* $2 \leq k_y \leq 4$. This Island of oscillation represents the stable linear structure of the rotating wave.

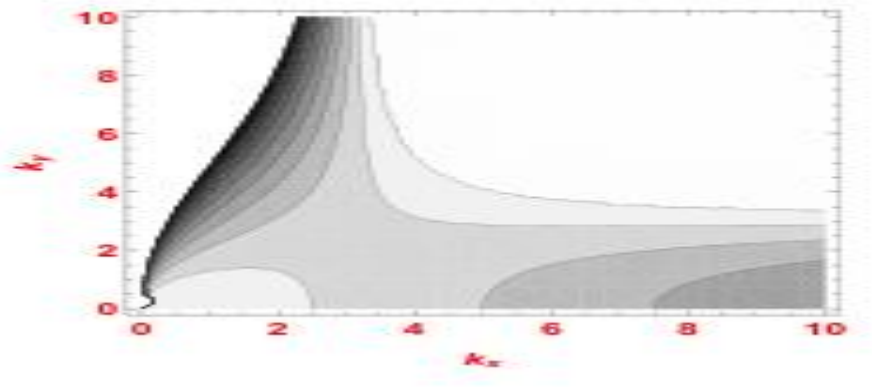

Figure 4: The contour plot of variation of the mode frequency ω over a range of parametric wave-number k_x and k_y generated from Eq. (15).

Using parameters describing above with appropriate boundary conditions (Simon *et. al.*, 2014; Rogers, 2008) and vorticity sources relevant to the confined GRS's vortex, the steady-state solutions of Eq. (22) are depicted in Fig. 5. For the sake of simplicity, we implement a circular domain with an aspect ratio of $L_y/L_x = 0.5$ that is appropriate to the GRS's current display size as specified in Rogers, 2008. In the domain, the GRS is a largely bounded quasi-steady circulation in the presence of stable streaming zonal jets, whose profile has a weak eastward peak at 26.5° S and a westward peak at 19.5° S. This could potentially be the cause of the GRS's horizontal drift

in a westward direction (Rogers, 2008). Fig. 5 shows the steady-state dust flow streamline patterns, which are the contours of ψ (on the left) and corresponding structure (on the right), in the latitude/longitude -plane. At a particular viscosity regime (Vidmachenko, 1986), the flow vorticity along the boundary is symmetric, uniformly diffuse, and relatively weak over the entire domain. The related streamline pattern is a circulation that follows the geometry of the confined GRS as illustrated. The dynamical changes have a relatively minimal impact on viscosity and are related to vorticities and zonal flow velocities. The dynamical regime, not the geometry of the confined domain, determines the state of the flow that retains more momentum or energy, and as a result, the flow structure changes rather slowly. Instead of diffusing directly towards the outer region, the vorticity close to the boundary can convect along the streamlines and then dissipate inside the vortex because of the relative increase in convective transport. The subsequent streamline patterns are circular and they transform into a new self-organized state with a circular core region surrounded by high speed collar layers that separate the core from the regions around it filled with thin and prolonged vortices.

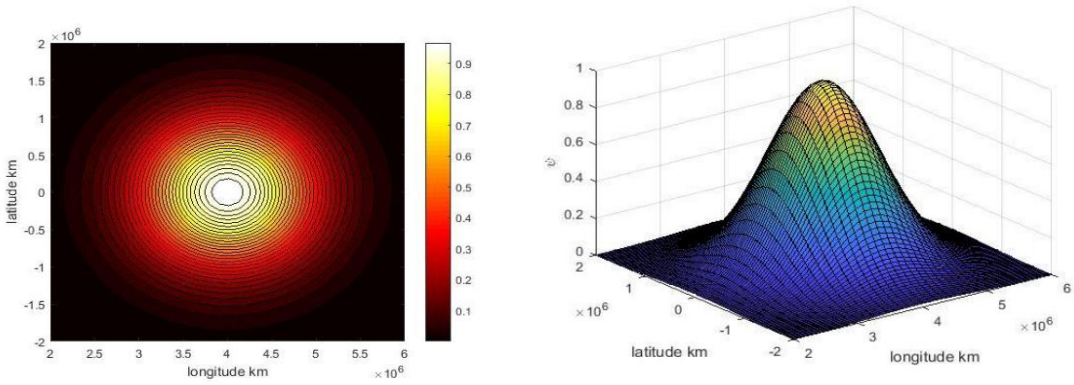

Figure 5: Numerical solution of Eq. (22) displays longitude, latitude, and steam functions (Contour on left and 3D on right) at zonal velocity scale 〖U〗_0=120 m/sec of the GRS.

Cross-section profiles of velocity U passing through the center of the circulation (x_0, y_0) against latitude are used to illustrate the structural changes at vorticity in the 10^{-1} to 10^{-6} s^{-1} range (top left is 10^{-1} to bottom right 10^{-6}) of the bounded dust flow in Fig. 5. We examined the mean wind shear (Wong et al., 2021) spanning the 20–25°S region in order to rule out the possibility that changes in the GRS velocity field were caused by changes in the vortex surrounds. The average wind speed in the high-speed ring and long-term variations in vortex size, shape, and wind shear do not show a monotonic shift in the wind shear. The non-dimensional Rossby number $R_0 =$

U_0/f_0L_0 is the relation between the strength of the inertial and Coriolis forces. We observed that the GRS's Rossby number did not correspond to long-term patterns. Because shear in the environment of vortices produces deviations from circular shape (e.g., Marcus, 1990; Moore & Saffman, 1971), a decrease in the amount of the anticyclonic shear in the surrounding flow could explain a long-term change in aspect ratio. Over the period 2009 to 2020, the environmental wind shear did not decrease. It is unclear whether the wind shear is increasing with time (which, in the absence of any other factors, would lengthen rather than circularize the GRS), or whether it changes in a more complex manner. The vorticity in the GRS outer region is analyzed to the profile shape of the velocity field across the ring (expressed by "decay factors") in order to rule out a prolonged changes in static stability. Increase in the amplitude of velocity profile is found for the lower value of vortices as shown in Fig. 6.

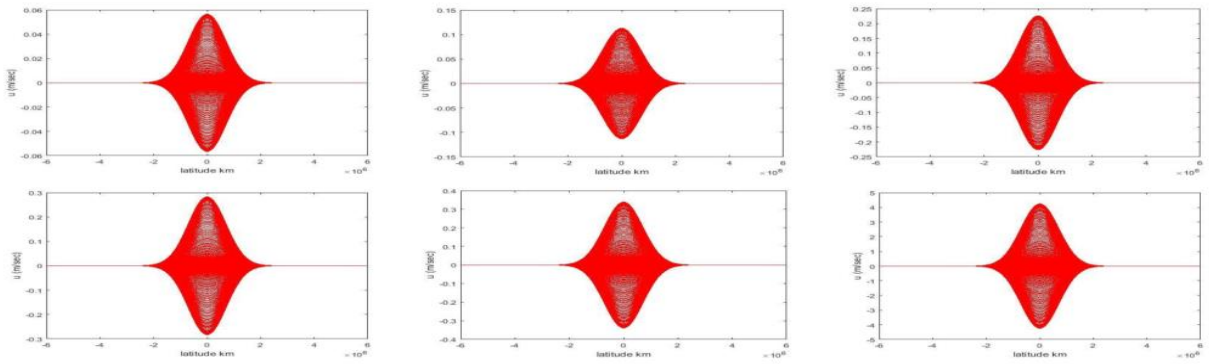

Figure 6: Cross-section profiles of steady flow velocity at vorticity in the 10−1 to 10−6 s−1 range (top left is 10−1 to bottom right 10−6).

The horizontal wind fields only cover a small range of altitudes. We presented the mathematical model to describe the structure, stability and shape of the vortex dynamics. Whereas, vortex models confined by imaging and wind field data have been widely employed to predict atmospheric static stability on Jupiter (Brueshaber & Sayanagi, 2021; Brueshaber et al., 2019; Cho et al., 2001; Shetty & Marcus, 2010).

4. Conclusion

The theoretical model we proposed in this work can interpret the turbulence behaviors at the GRS region and describes particle dynamics that are identical to those of the real Jupiter's atmosphere.

One noteworthy drawback of this model is its 2D representation, although real 3D effects from the interior could be anticipated (Ingersoll et al., 2000). The wave dispersion is seen in the linear analysis. In stable vortex-flows minimal effect of kinematics viscosity is demonstrated. The linear and nonlinear solution illustrates a crucial wave process by which perturbation can take energy out of the vortex at one band and deposit it at another. Depending on the shear characteristics of the zonal jets, the vortices in the entire banded structure in atmosphere of Jupiter vary in size, strength, and direction. The vortices also have additional impacts from the Coriolis force that may actually strengthen or decrease the absolute vorticity. These parameters provide work frame to the argument that the streaming zonal jets are the predominant driver of the vortices. In short, the present study has shown that rather than kinematic viscosity, changes in properties related to zonal jets, driving fields, and vorticity are responsible for many observed characteristic aspects of Jupiter's vortices, particularly the vortex dynamics of GRS.

Data availability statement

All data that support the findings of this study are included within the article.

Conflict of interest

The authors have no conflicts to disclose.

References

Asay-Davis, X. S., Marcus, P. S., Wong, M. H., & de Pater, I. 2009. Jupiter's shrinking Great Red Spot and steady Oval BA: Advection Corrected Correlation Image Velocimetry' automated cloud-tracking method. Icarus 203(1), 164–188.

Asay-Davis, X. S. 2015. Corrected Correlation Image Velocimetry (ACCIV). GitHub Code Repository.

Barnes, M. S., Keller, J. H., Forster, J. C., ONeill, J. A. and Coultas, D. K. 1992. Transport of dust particles in glow-discharge plasmas. Phys. Rev. Lett. 68, 313.

Barkan, A., D'Angelo N., and Merlino, R.L. 1995 Charging of Dust Grains in a Plasma. Phys. Rev. Lett. 73, 3093

Bhimsen, K. SHIVAMOGGI. 1989. CHARNEY-HASEGAWA-MIMA EQUATION: A GENERAL CLASS OF EXACT SOLUTIONS. Physics Letters A 138.

Brueshaber, S. R., & Sayanagi, K. M. 2021. Effects of forcing scale and intensity on the emergence and maintenance of polar vortices on Saturn and Ice Giants. Icarus, 361, 114386. (18pp).

Brueshaber, S. R., Sayanagi, K. M., & Dowling, T. E. 2019. Dynamical regimes of giant planet polar vortices. Icarus, 323, 46–61.

Cho, J. Y.-K., de la Torre Juárez, M., Ingersoll, A. P., & Dritschel, D. G. 2001. A high-resolution, three-dimensional model of Jupiter's Great Red Spot. Journal of Geophysical Research, 106(E3), 5099–5106.

Choi, D. S., Showman, A. P. and Vasavada, A. R. 2010. The evolving flow of Jupiter's White Ovals and adjacent cyclones. Icarus 207, 359.

Dressel, L. 2021. Wide Field Camera 3 Instrument Handbook, Version 13.0. Space Telescope Science Institute.

Dowling, T. E. and Ingersoll, A. P. 1989. Jupiter's Great Red Spot as a shallow water system. J. Atmos. Sci. 46, 3256.

Groves, M.D. and Sun, S.M. 2008. Fully localised solitary-wave solutions of the threedimensional gravity–capillary water-wave problem, Arch. Ration. Mech. Anal. 188, 1–91.

Infeld, E. and Rowlands, G. 2001. Nonlinear Waves, Solitons and Chaos, Cambridge University Press.

Guinn, T. A. and Schubert, W. H. 1993. Hurricane spiral bands. J. Atmos. Sci., 50, 3380-3403.

Gent, P. R. and McWilliams J. C. 1986. The instability of barotropic circular vortices. Geophysical & Astrophysical Fluid 35, 209-235.

Hueso, R., Sánchez-Lavega, A., Rojas, J. F., Simon, A. A., Barry, T., del Río-Gaztelurrutia, T., et al. 2020. Saturn atmospheric dynamics one year after Cassini: Long-lived features and time variations in the drift of the Hexagon. Icarus, 336, 23.

Ingersoll, A. P., Gierasch, P. J. Banfield, D., Vasavada, A. R., and Team, G. I. 2000. Moist convection as an energy source for the large-scale motions in Jupiter's atmosphere. Nature 403, 630.

Ivlev, A. V., Khrapak, S. A. Zhdanov, S. K., Morfill, G. E., and Joyce, G. 2004. Force on a charged test particle in a collisional flowing plasma. Phys. Rev. Lett. 92, 205007.

Khrapak, S. A., Ivlev, A. V. Morfill, G. E., and Thomas, H. 2002. Ion drag force in complex plasmas. M. Phys. Rev. E 66, 046414.

Kadomtsev, B.B. and Petviashvili, V.I. 1970. On the stability of solitary waves in weakly dispersive media, Sov. Phys. Dokl. 15, 539–541.

Liu, Q., Zhang, R., Yang, L., Song, J. 2018. A new model equation for nonlinear Rossby waves and some of its solutions. Physics Letter A 383, 514-525.

Landau, L. D. and Lifshits, E. M. 1987. Fluid Mechanics (PergamonPress, Oxford, England.

Loeffler, M. J., Hudson, R. L., Chanover, N. J., and Simon, A. A. 2016. The spectrum of Jupiter's Great Red Spot: The case for ammonium hydrosulfide (NH4SH). Icarus 271, 265.

Marcus, P. S. 1993. Numerical simulation of jupiter's great red spot. *Nature (London)* ***331***, 693.

Marcus P. S. 1993. Jupiter's Great Red Spot and other vortices. *Annu. Rev. Astron. Astrophys.* ***31***, 523.

Marcus, P. S. 2004. Prediction of a global climate change on Jupiter. Nature, 428(6985), 828–831.

Marcus, P. S. and Shetty, S. 2011. Jupiter's zonal winds: are they bands of homogenized potential vorticity organized as a monotonic staircase? Phil. Trans. R. Soc. A 369, 771.

Marcus, P. S. and Lee, C. 1994. Jupiter's Great Red Spot and zonal winds as a self-consistent, one-layer, quasigeostrophic flow. Quasigeostrophic flow Chaos 4, 269.

Moore, D. W., & Saffman, P. G. 1971. Structure of a Line Vortex in an Imposed Strain. In J. H. Olsen, A. Goldburg, & M. Rogers (Eds.), Aircraft wake turbulence and its detection.

Marcus, P. S. 1990. Vortex dynamics in a shearing zonal flow. Journal of Fluid Mechanics, 215, 393–430.

Mitchell, J. L., Beebe, R. F., Ingersoll, A. P. and Garneau, G. W. 1981. Flow fields within Jupiter's great red spot and white oval BC. J. Geophys. Res. 86, 8751.

Rehman, U., Hussain, I., and Qammar, A. 2022. On the potential variation of charged dust in Saturn's magnetosphere: The dust-plasma interaction. Planetary and Space Science 223, 105577.

Rogers, J. H. 2008. The accelerating circulation of Jupiter's Great Red Spot. J. Br. Astron. Assoc. 118.

Simon, A. A., Wong, M. H., Rogers, J. H., Orton, G. S. de Pater, I., Asay-Davis, X., Carlson, R. W., and Marcus, P. S. 2014. DRAMATIC CHANGE IN JUPITER'S GREAT RED SPOT FROM SPACECRAFT OBSERVATIONS. ApJL 797 L31.

Simon, A. A., Tabataba-Vakili, F. Cosentino, R., Beebe, R. F., Wong, M. H. and Orton,G. S. 2018. Historical and Contemporary Trends in the Size, Drift, and Color of Jupiter's Great Red Spot. The Astronomical Journal 155, 151.

Simon-Miller, A. A., Gierasch, P. J., Beebe, R. F. Conrath, B., Flasar, F., and Achterberg, R. K. 2002. New observational results concerning Jupiter's great red spot. Icarus 158, 249.

Sun, B., Liu, C., & Wang, F. 2018. Global meridional eddy heat transport inferred from Argo and altimetry observations. Scientific Reports, 9, 1345.

Sayanagi, K. M., Dyudina, U. A., Ewald, S. P., Fischer, G., Ingersoll, A. P., Kurth, W. S., et al. 2013. Dynamics of Saturn's great storm of 2010-2011 from Cassini ISS and RPWS. Icarus, 223(1), 460–478.

Simon, A. A. 2015. Outer Planet Atmospheres Legacy ("OPAL"). Barbara A. Mikulski Archive for Space Telescopes, Dataset.

Shetty, S., & Marcus, P. S. 2010. Changes in Jupiter's Great Red Spot (1979-2006) and Oval BA (2000-2006). Icarus, 210(1), 182–201.

Vidmachenko, A. P. 1986. Some dynamical parameters of the atmosphere of Jupiter. Kinematics and Physics of Celestial Bodies 2, 54-56.

Vasavada, A. R., Ingersoll, A. P. D. Banfield, Bell, M., Gierasch, P. J., Belton, M. J., Orton, G. S., Klaasen, K., DeJong, P. E., Breneman, H. T., Jones, J., Kaufman, J. M., Magee, K. P. and Senske,

D. A. 1998. Galileo Imaging of Jupiter's Atmosphere: The Great Red Spot, Equatorial Region, and White Ovals. *Icarus, **135***, 265.

Wong, M. H., Marcus, P. S., Simon, A. A., de Pater, I., Tollefson, J. W., & Asay-Davis, X. 2021. Evolution of the horizontal winds in Jupiter's Great Red Spot from one Jovian year of HST/WFC3 maps. Geophysical Research Letters, 48, e2021GL093982.

Weidenschilling, S. and Lewis, J. 1973. Atmospheric and cloud structures of the Jovian planets. Icarus 20, 465.

Zakharov, V.E and Kuznetsov, E.A. 1974. On three-dimensional solitons, Sov. Phys. 39 (2), 285–286.

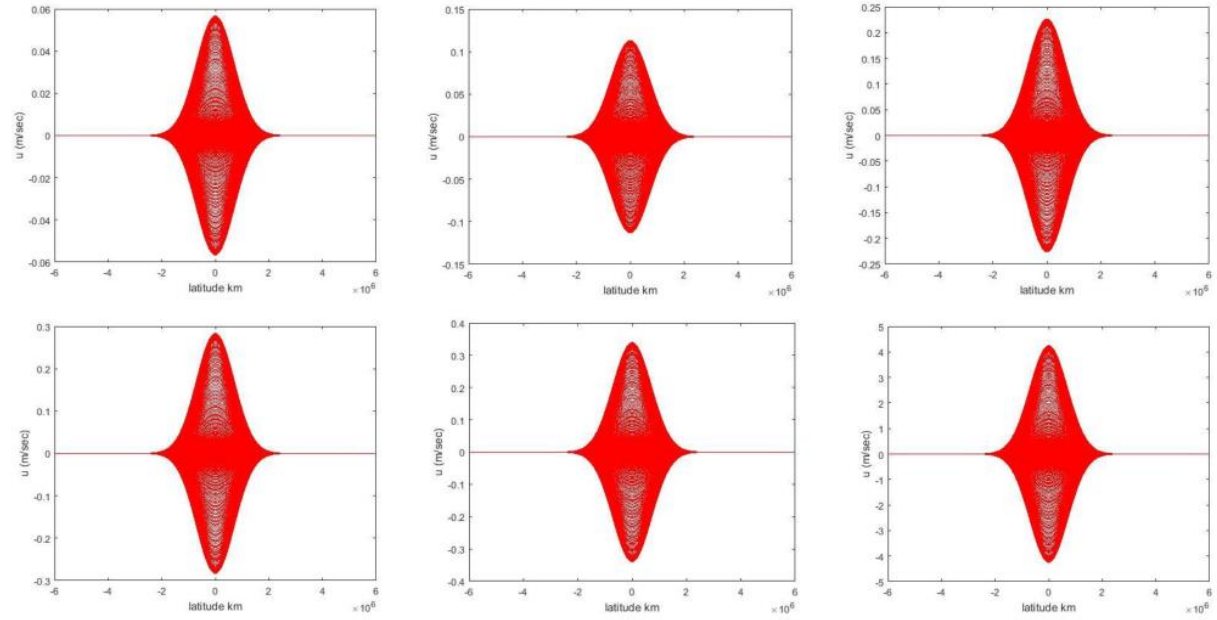
u (m/sec)
latitude km
×10^6